Signal Integrity Verification of Multi-Chip Links using Passive Channel Macromodels

Alessandro Chinea, Stefano Grivet-Talocia, *Senior Member, IEEE,* Haisheng Hu, Piero Triverio, *Member, IEEE*, Dierk Kaller, Claudio Siviero, Martin Kindscher

***Abstract*—This paper presents a general strategy for the electrical performance and Signal Integrity assessment of electrically long multi-chip links. A black-box time-domain macromodel is first derived from tabulated frequency responses in scattering form. This model is structured as a combination of ideal delay terms with frequency-dependent rational coefficients. A new identification scheme is presented, based on an initial blind delay estimation process, followed by a refinement loop based on an iterative Delayed Vector Fitting (DVF) process. Two alternative passivity enforcement schemes based on local perturbations are then presented. The result is an accurate and guaranteed passive delay-based macromodel, which is synthesized as a SPICE-compatible netlist for channel analysis. The proposed procedure enables safe and reliable circuit-based transient simulations of complex multi-chip links, including nonlinear drivers and receivers. The performance of the proposed flow is demonstrated on a large number of channel benchmarks.**

***Index Terms*—Macromodeling, Rational Approximations, Delay Extraction, Passivity, Scattering Parameters, High-Speed Interconnects**

I. Introduction

This paper is about electrical modeling of high-performance chip-to-chip interconnects for Signal Integrity verifications [1], [2], [3], [4], [5], [6]. Two main challenges must be faced in the numerical simulation of such structures. First, the electrical length of the link may be considerable, since the spectral content of high-speed digital signals in modern designs reaches the multi-GHz range, and the corresponding minimum wavelength of propagating fields may be a small fraction of the overall link length. Thus, electrical models taking into account the distributed nature of the link and the inevitable propagation delays are mandatory [18]–[25]. Second, the signals may undergo several discontinuities along their propagation, coming from vias, connectors, or return path discontinuities due to routing constraints or irregular power/ground planes at the package and board level. Spurious signal reflections may arise, which must be correctly represented in electrical models [8]–[17].

A standard modeling approach is to characterize the entire link in the frequency domain, in order to accurately represent all signal degradation effects, including frequency-dependent metal and dielectric losses. Each elementary block forming the interconnect is analyzed separately via full-wave tools. Pure transmission-line segments are characterized via 2D solvers, whereas via fields, connectors and lumped discontinuities are analyzed via 3D techniques. As a result, the overall response of the entire chip-to-chip link is obtained by cascading the different blocks at each individual frequency in the range of interest, leading to a set of tabulated frequency responses typically in scattering form. The same description may be obtained, when feasible, via direct measurement using a multiport Vector Network Analyzer (VNA).

Frequency-domain analysis is straightforward once the above information is available. Standard FFT methods may then be used to recover the time-domain impulse or step responses, which in turn may be processed to derive global metrics such as eye diagram openings or Bit Error Rate (BER) statistics [4], [5], [6], [7]. The main drawback of this approach is in the intrinsic assumption of linearity. Nonlinear models for drivers and receivers cannot be used, thus limiting the scope and the representativeness of the results.

This work presents a different approach. Building on various existing results, a time-domain macromodeling procedure is presented. The raw tabulated frequency responses are fed to a delay-rational identification scheme, which produces a parametric closed-form model. This model is successively processed by a passivity check and enforcement procedure and synthesized as a SPICE-compatible netlist. Due to the passivity constraint, this model can be safely employed in transient analysis [27], [28], including accurate nonlinear models of drivers and receivers.

There are various new contributions in this work. First, a new blind delay identification technique is presented. When combined with an iterative application of Delayed Vector Fitting (DVF), this technique proves superior in its accuracy or greatly simplified in its implementation with respect to previous solutions. Second, two passivity enforcement schemes are reviewed and extended to DVF macromodels, together with optimality constraints based on suitable weighted norms for accuracy preservation. Third, a systematic application to several benchmarks of industrial interest has been performed and is documented in this paper. The excellent results that are achieved on all cases demonstrate the robustness of the proposed flow.

II. Delay-Rational Macromodels

We consider a generic chip-to-chip link with P electrical ports. The structure is known via its sampled scattering matrix

Manuscript received ; revised.

Alessandro Chinea, Stefano Grivet-Talocia, Haisheng Hu, and Piero Triverio are with the Department of Electronics, Politecnico di Torino, Torino 10129, Italy (e-mail: alessandro.chinea@polito.it; stefano.grivet@polito.it; haisheng.hu@polito.it; piero.triverio@polito.it); Dierk Kaller, Claudio Siviero, and Martin Kindscher are with IBM Systems and Technology Group, IBM Deutschland Research & Development GmbH, Böblingen 71032, Germany (e-mail: dkaller@de.ibm.com; csiviero@de.ibm.com; kindsche@de.ibm.com)

$\widehat{\boldsymbol{S}}_l \in \mathbb{C}^{P\times P}$ at the discrete frequencies $\omega_l,\ l = 1,\ldots,L$. This type of characterization has become very popular due to the availability of the Touchstone standard [50]. Our main objective is to derive a closed-form black-box macromodel $\boldsymbol{S}(s)$ that

1) matches the raw data over the available bandwidth, i.e., $||\boldsymbol{S}(j\omega_l) - \widehat{\boldsymbol{S}}_l|| < \varepsilon$, where ε is a predefined accuracy threshold;
2) is guaranteed passive;
3) allows closed-form conversion to time-domain (e.g., via analytic Laplace transform inversion) and/or synthesis as an equivalent circuit that can be interpreted and processed by standard circuit solvers of the SPICE class;
4) is efficient in SPICE-based transient simulations.

It has been proved in [23] that the scattering responses of any complex and electrically long interconnect can be represented by linear combinations of delay operators with rational coefficients. This naturally leads to the Delay-Rational Macromodel (DRM) structure, defined as

$$\boldsymbol{S}(s) = \sum_{m=1}^{M} \boldsymbol{Q}_m(s) e^{-s\tau_m}\,, \tag{1}$$

where s is the Laplace variable, τ_m are delays corresponding to the various arrival times of the signal reflections induced by an input unit pulse, and

$$\boldsymbol{Q}_m(s) = \sum_{n=1}^{N_m} \frac{\boldsymbol{R}_{mn}}{s - p_{mn}} + \boldsymbol{Q}_{m,\infty} \tag{2}$$

are matrix rational coefficients representing other effects such as attenuation and dispersion. The time-domain representation of (1) is a weighted sum of delayed exponentials, so condition 3) above is fulfilled by construction. The rest of this paper will present a modeling flow providing a good solution to conditions 1), 2) and 4).

III. Identification of Delay-Rational Macromodels from Tabulated Data

The identification of (1) from the samples $\widehat{\boldsymbol{S}}_l$, i.e., solving

$$\min ||\boldsymbol{S}(j\omega_l) - \widehat{\boldsymbol{S}}_l||\,, \tag{3}$$

where the minimum is taken over the unknown delays τ_m and matrix rational functions $\boldsymbol{Q}_m(s)$ is a very challenging task. The solution to this problem is not even unique, since the delay operator $e^{-s\tau_m}$ can be represented itself via a (possibly high-order) rational function. Actually, the (delayless) case $M = 1$, $\tau_1 = 0$ provides a simpler and purely rational model structure, for which direct application of standard macromodeling schemes such as Vector Fitting [8], [10] may lead to quite good results as far as accuracy is concerned. Such models are however characterized by excessively high orders for long channels, since many poles are required to reproduce the fast phase variations induced by the delay operators [19]–[20]. Since our aim is to maximize model efficiency, condition 4) above, we rule out this choice.

Good solutions for the identification of DRM's via Delayed Vector Fitting (DVF) or Delayed Sanathanan-Koerner (DSK) iterations are available, see [23]. However, these methods provide good results only when a sufficiently accurate estimate for the dominant delays is available. In other words, a preliminary (blind) identification of the delays τ_m is necessary as a preprocessing step for the rational approximation stage. Being open-loop, this strategy may not be optimal, since the success of the rational approximation is highly sensitive to the accuracy of the delay estimates. Some approaches to correct the delay estimates are only available for simple cases [31], [32] and are not applicable in the general case.

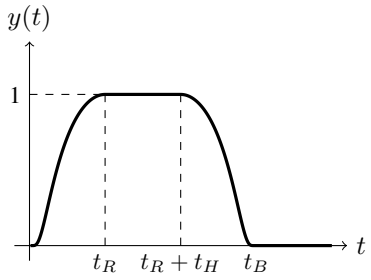

Fig. 1. Waveform of the input pulse used for the estimation of the delays.

In order to avoid these difficulties, we first implemented a closed-loop delay-rational identification algorithm. In this scheme, the rational approximation step is performed via DVF [23] and is embedded in an outer loop that optimizes the delay estimates using the Nelder-Mead simplex method [43]. Although some improvement was observed in some cases, this technique was not found to be robust for general application. An example will be provided in Section III-B. The main reason is the lack of a sound and automated criterion for defining both the number of required delays and a sufficiently narrow search area for their values.

In order to circumvent such issues, we have developed a new algorithm for blind delay estimation, which is presented in Section III-A. This algorithm provides a superset of accurate candidate delays estimates with an associate ranking. The latter is exploited within an incremental refinement loop based on DVF, documented in Section III-B. The resulting scheme does not require nonlinear optimizations and provides excellent accuracy and robustness, as will be demonstrated in Section VI.

A. Blind Estimation of Dominant Delays

In this section, we describe a blind delay estimation algorithm for the direct identification of the dominant delays τ_m from the available frequency samples. The proposed technique is based on a simple analysis of the time-domain response to a bandlimited pulse, defined as

$$x(t) = \begin{cases} \exp\left(-\frac{\eta_1(t)^2}{1-\eta_1(t)^2}\right) & \text{if } 0 \leqslant t < t_R, \\ 1 & \text{if } t_R \leqslant t < t_R + t_H, \\ \exp\left(-\frac{\eta_2(t)^2}{1-\eta_2(t)^2}\right) & \text{if } t_R + t_H \leqslant t < t_B, \\ 0 & \text{if } t \geqslant t_B, \end{cases} \tag{4}$$

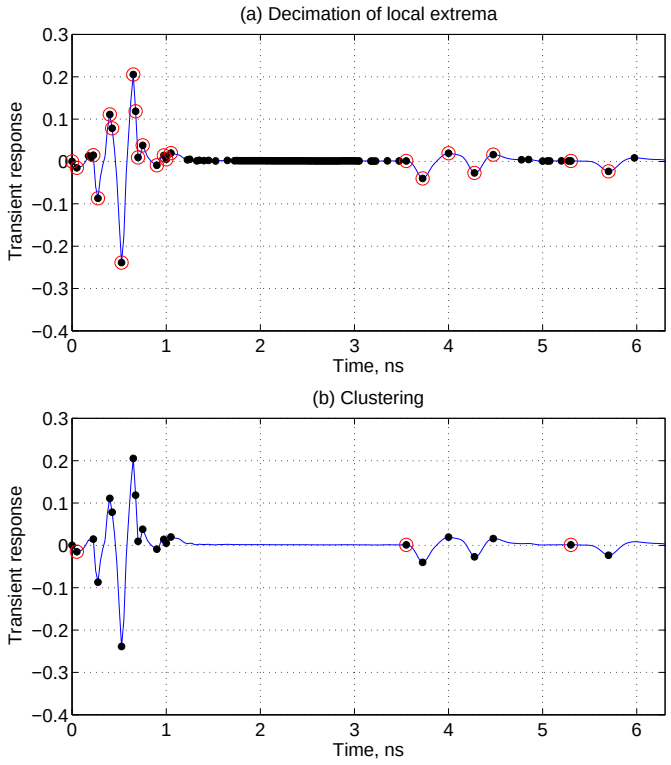

Fig. 2. Illustration of the blind delay extraction process on a sample response. In (a), black dots denote the set $\mathcal{P}$ and circles highlight the downselected set $\widehat{\mathcal{P}}$. In (b), black dots denote the set $\widehat{\mathcal{P}}$ and circles highlight the dominant delays in $\widetilde{\mathcal{P}}$. See also text.

with

$$\eta_1(t) = \frac{t - t_R}{t_R}, \qquad \eta_2(t) = \frac{t - t_R - t_H}{t_R}, \tag{5}$$

where t_R is the rise time, t_H is the pulse width and $t_B = 2t_R + t_H$, see Fig. 1. A simple check shows that the function $x(t)$ belongs to the class $\mathcal{C}_0^\infty$, i.e., the set of infinitely differentiable functions with compact support [45]. These functions have a very narrow bandwidth, in particular, the spectrum $X(\omega)$ of $x(t)$ decays faster than any finite power of $1/\omega$. It is thus possible to determine the actual values for t_R and t_H such that $X(\omega) < \epsilon$ with any arbitrarily small ϵ for frequencies $\omega > \omega_{\max}$ beyond the maximum available frequency in the raw data. This condition guarantees that this pulse does not excite any frequency content for which no data is available.

Application of the pulse $x(t)$ to the j-th port of the channel leads to a transient response $y_{ij}(t)$ at the i-th port. For simplicity, we will omit all subscripts throughout this section, assuming a generic input-output response of the channel $y(t)$. This response is reliably computed via Inverse Fast Fourier Transform (IFFT). Since any scattering response is unitary bounded $|S(j\omega)| \leq 1$, we have $|Y(\omega)| = |S(j\omega)X(\omega)| < \epsilon$ for $\omega > \omega_{\max}$. Application of IFFT is therefore safe, since aliasing or truncation effects are minimized [46].

Estimation of the delays is performed via the following simple steps. Note that three thresholds $\{\gamma, \alpha, \beta\}$ are used to parameterize the algorithm, as discussed below.

1) The locations of all local minima and maxima of $y(t)$ are collected in the set $\mathcal{P} = \{t_m\}$, including the starting point $t_0 = 0$. The pulse response $y(t)$ is thus monotonic within each interval (t_m, t_{m+1}).
2) For each interval (t_m, t_{m+1}), the largest t_m^* such that $|y(t_m^*) - y(t_m)| < \gamma \max_m |y(t_{m+1}) - y(t_m)|$ is added to the set $\mathcal{P}$, where $0 < \gamma < 1$, and the set $\mathcal{P}$ is re-sorted. This step adaptively increases the number of samples, making sure that each large transition edge includes at least one sample. A graphical illustration of set $\mathcal{P}$ is provided by the black dots in Fig. 2(a).
3) A new set $\widehat{\mathcal{P}}$ is constructed by extracting the points t_m from $\mathcal{P}$ such that $\delta_m > \alpha\delta_{\max}$, where $\delta_m = |y(t_{m+1}) - y(t_m)|$, $\delta_{\max} = \max_m\{\delta_m\}$, and $0 < \alpha < 1$. This process guarantees that local extrema that are characterized by small variations with respect to their neighbors are rejected. Only the extrema corresponding to significant "jumps" with respect to their neighbors are retained. The elements in set $\widehat{\mathcal{P}}$ are highlighted with circles in Fig. 2(a), and depicted as black dots in Fig. 2(b).
4) Since the bandlimited nature of the pulse $x(t)$ provides a limited time-domain resolution, which is roughly equivalent to the center of the pulse $t_B/2$, we reject the time points that are "too close" to their neighbors. More precisely, we form a new set $\widetilde{\mathcal{P}}$ collecting all time points $t_m \in \widehat{\mathcal{P}}$ that fulfill the condition

$$|t_m - t_{m-1}| > \beta \frac{t_B}{2}, \tag{6}$$

where $\beta > 1$. The remaining points t_m are further ranked according to the metric $|t_m - t_{m-1}|$, and the $M_{\max}$ corresponding to the highest rank are selected. The elements in set $\widetilde{\mathcal{P}}$ are highlighted by circles in Fig. 2(b). The set of delay estimates to be used for DVF application is obtained by removing from these points the bias induced by the center of the pulse as

$$\tau_m := t_m - \frac{t_B}{2}. \tag{7}$$

Some comments about this process are in order. We first remark the simplicity of this algorithm. This scheme is far less complicated that the Gabor transform approach of [19] or the Wavelet transform approach of [25]. However, the main features of the latter are retained in the proposed scheme, since both approaches do perform some sort of singularity analysis of the waveforms. The approach in [25] obtains candidate delays by thresholding small-scale wavelet coefficients, which correspond to nearly singular points, followed by a clustering process. Our approach performs a discrete form of singularity analysis (steps 1–3), which is performed on the extrema of a bandlimited smoothed response, thus intrinsically less sensitive to noise. Clearly, step 4 above is equivalent to a clustering process, similar to the approach of [25]. Furthermore, the suggested ranking process downselects as dominant delays those corresponding to largest distances with respect to their preceding neighbors. This ranking is very effective in optimizing the model structure, since it avoids pairs of nearby delays, which may lead to numerical ill-conditioning of

TABLE I
MACROMODELING RESULTS FROM DO-DVF AND I-DVF ALGORITHMS

	RMS Error $\times 10^{-3}$		CPU time (s)	
	DO-DVF	I-DVF	DO-DVF	I-DVF
$S_{1,1}$	9.64	6.67	50.27	6.29
$S_{1,5}$	2.61	0.55	29.67	5.58
$S_{1,6}$	0.37	0.14	11.71	3.46
$S_{1,11}$	1.23	0.57	10.53	2.96
$S_{1,17}$	0.38	0.17	18.69	4.88

the DVF algorithm without significant improvement in model accuracy.

The various steps above depend on suitable choices for the three thresholds $\{\gamma, \alpha, \beta\}$. In order to determine optimal values for these thresholds, the algorithm was run on a large number of test cases (see Section VI) by varying the thresholds. The values $\gamma = 0.3$, $\alpha = 0.02$, $\beta = 5$ provided the best results in all cases. These optimal values are therefore used for all numerical results of this paper.

B. Iterative Delay-Rational Model Identification

The blind delay estimation algorithm of Section III-A generates a set of $M_{\max}$ candidate delays τ_m, which are sorted based on their ranking. The actual number of delays that is required for fitting a given response is obtained as a compromise between model accuracy and complexity. This is achieved via the following simple iterative refinement loop

1) Set M = 1
2) Perform a DVF run [23] using τ_m, $m = 1, \ldots, M$ and evaluate the time-domain response $\hat{y}(t)$ of the resulting model to the input pulse (4)
3) Compute the time t^* where the model vs data error $\epsilon(t) = |\hat{y}(t) - y(t)|$ is maximum.
4) If $\epsilon(t^*)$ is less than a prescribed threshold exit, otherwise set $M := M + 1$ and go to step 2).

In the actual implementation, the refinement loop is interrupted also when a maximum number of delays $\bar{M}$ is reached. This value is set to $\bar{M} = 5$ in all examples of this paper. In case $M_{\max} < \bar{M}$, the set of delays in step 4) is increased by adding the element in set $\mathcal{P}$ (less the bias $t_B/2$) that results closest to the maximum error location t^*. Also, the zero-delay is explicitly included for all reflections and near-end crosstalk responses since the first iteration step. Due to its iterative nature, this scheme is denoted in the following as Iterative DVF (I-DVF).

The performance of the I-DVF scheme is now compared to another DVF implementation, which performs a direct optimization of the delays τ_m via the Nelder-Mead simplex method [43]. Each step of the optimization loop consists of a plain DVF run as in [23]. The starting set of delays for the optimization is also constructed as described in [19]. This scheme is denoted in the comparison as Direct Optimization DVF (DO-DVF). The comparison is presented here using a representative test case (a 18-port channel connecting a CPU to an I/O card), noting that similar results were obtained for all the benchmarks that will be presented in Section VI.

Table I shows the main results. Each row in the table reports a comparison between the two algorithms. The proposed I-DVF scheme always provides a better accuracy in terms of RMS fitting error. Also, the CPU time required by the overall identification is drastically reduced, because of the improved initial choice of the dominant delays. In order to provide a good fit, the DO-DVF requires a nonlinear optimization loop on the delay values, which in turn requires a large number of DVF runs before some optimum is found. Only a limited number of DVF runs is instead required by I-DVF, since no modification of the delay estimates is necessary through the iterations.

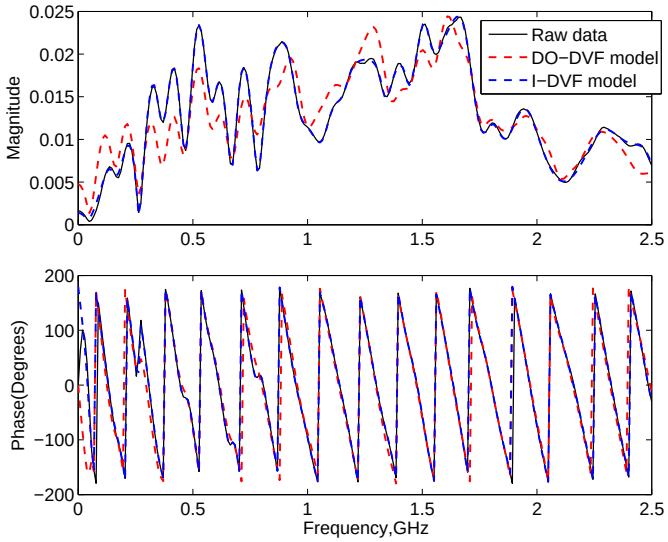

Fig. 3. Frequency-domain comparison between model and data for the crosstalk $S_{1,4}$ of a complex channel. Only a reduced bandwidth of 5 GHz is depicted for readability.

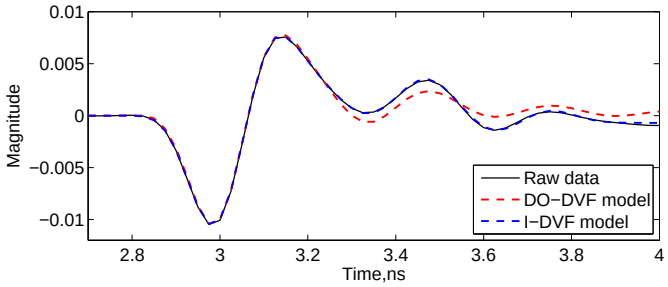

Fig. 4. As in figure 3, but in time-domain.

Figure 3 shows the frequency domain fitting result for a far end crosstalk $S_{1,4}$ for both algorithms, and Fig. 4 depicts the corresponding macromodel responses to the same input pulse (4), together with the raw response $y(t)$ computed from the data via FFT. In both frequency and time domain, the improvement in accuracy is clearly visible.

IV. PASSIVITY CHARACTERIZATION

Electrical interconnects are physically passive, i.e., they are unable to generate energy. Mathematical models in form (1) may however lose this property due to numerical approximations in the identification process. Unfortunately, non-passive macromodels may lead to unstable results when used

in transient simulations, even when their terminations are passive [28], [27]. Therefore, the model must be checked for passivity and, if passivity is violated within some frequency bands, a suitable passivity enforcement process must be applied. To this end, we recall that a delayed state-space realization

$$\boldsymbol{S}(s) = \left(\sum_{m=1}^{M} \boldsymbol{C}_m e^{-s\tau_m} \right) (s\boldsymbol{I} - \boldsymbol{A})^{-1} \boldsymbol{B} + \boldsymbol{D} \tag{8}$$

may be derived from (1) using standard methods [24]. This will be our starting point in this section.

We assume that all poles of all matrix rational coefficients $\boldsymbol{Q}_m(s)$ have a strictly negative real part. This is enforced by any standard rational identification scheme such as VF, DVF, or DSK [23]. In addition, we assume that $\boldsymbol{Q}_m(s)$ is strictly proper whenever the associated delay $\tau_m \neq 0$. Under these assumptions, it can be shown [33] that the model (8) is passive when

$$(\boldsymbol{I} - \boldsymbol{S}^H(j\omega)\boldsymbol{S}(j\omega)) \geqslant 0, \quad \forall \omega \tag{9}$$

or, equivalently, when all the singular values of $\boldsymbol{S}(j\omega)$ do not exceed one at any frequency.

A direct check of (9) requires the evaluation of the singular values of $\boldsymbol{S}(j\omega)$ for many values of ω. An alternative and purely algebraic test condition was derived in [33] in form of a frequency-dependent eigenvalue problem. This result generalizes the approaches adopted in [29] for delayless models and in [35] for delayed models or transmission lines based on the Generalized Method of Characteristics (GMoC). The main theorem in [33] asserts that the imaginary eigenvalues of

$$\boldsymbol{H}(s)\boldsymbol{\xi} = s\boldsymbol{\xi} \tag{10}$$

correspond to the points where one of the singular values of $\boldsymbol{S}(j\omega)$ crosses the unit threshold. Therefore, if there are no purely imaginary solutions to (10), the model is passive. The complex matrix $\boldsymbol{H}(s)$ turns out to have Hamiltonian structure and is defined as

$$\begin{aligned} \boldsymbol{H}(s) = \boldsymbol{\mathcal{V}} &+ \sum_{m=1}^{M} \left(\boldsymbol{\mathcal{W}}_m^{+} e^{s\tau_m} + \boldsymbol{\mathcal{W}}_m^{-} e^{-s\tau_m} \right) \\ &+ \sum_{m,n=1}^{M} \boldsymbol{\mathcal{W}}_{m,n} e^{s(\tau_m - \tau_n)} \end{aligned} \tag{11}$$

where

$$\boldsymbol{\mathcal{V}} = \begin{bmatrix} \boldsymbol{A} & \boldsymbol{0} & \boldsymbol{B}\boldsymbol{R}\boldsymbol{B}^T & \boldsymbol{B}\boldsymbol{R}\boldsymbol{B}^T \\ \boldsymbol{0} & \boldsymbol{A} & \boldsymbol{B}\boldsymbol{R}\boldsymbol{B}^T & \boldsymbol{B}\boldsymbol{R}\boldsymbol{B}^T \\ \boldsymbol{0} & \boldsymbol{0} & -\boldsymbol{A}^T & \boldsymbol{0} \\ \boldsymbol{0} & \boldsymbol{0} & \boldsymbol{0} & -\boldsymbol{A}^T \end{bmatrix} \tag{12}$$

$$\boldsymbol{\mathcal{W}}_m^{+} = \begin{bmatrix} \boldsymbol{0} & \boldsymbol{0} & \boldsymbol{0} & \boldsymbol{0} \\ \boldsymbol{0} & \boldsymbol{0} & \boldsymbol{0} & \boldsymbol{0} \\ \boldsymbol{0} & \boldsymbol{0} & \boldsymbol{0} & \boldsymbol{0} \\ \boldsymbol{0} & \boldsymbol{0} & -\boldsymbol{C}_m^T \boldsymbol{D}\boldsymbol{R}\boldsymbol{B}^T & -\boldsymbol{C}_m^T \boldsymbol{D}\boldsymbol{R}\boldsymbol{B}^T \end{bmatrix} \tag{13}$$

$$\boldsymbol{\mathcal{W}}_m^{-} = \begin{bmatrix} \boldsymbol{0} & \boldsymbol{B}\boldsymbol{R}\boldsymbol{D}^T\boldsymbol{C}_m & \boldsymbol{0} & \boldsymbol{0} \\ \boldsymbol{0} & \boldsymbol{B}\boldsymbol{R}\boldsymbol{D}^T\boldsymbol{C}_m & \boldsymbol{0} & \boldsymbol{0} \\ \boldsymbol{0} & \boldsymbol{0} & \boldsymbol{0} & \boldsymbol{0} \\ \boldsymbol{0} & \boldsymbol{0} & \boldsymbol{0} & \boldsymbol{0} \end{bmatrix} \tag{14}$$

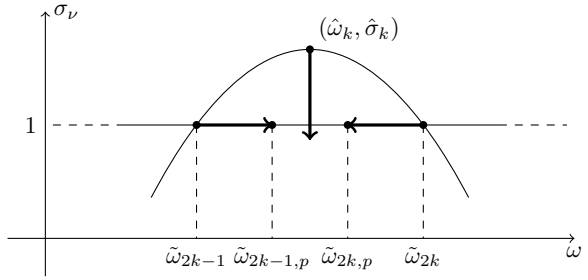

Fig. 5. Notation used in vertical and horizontal displacement algorithms.

$$\boldsymbol{\mathcal{W}}_{m,n} = \begin{bmatrix} \boldsymbol{0} & \boldsymbol{0} & \boldsymbol{0} & \boldsymbol{0} \\ \boldsymbol{0} & \boldsymbol{0} & \boldsymbol{0} & \boldsymbol{0} \\ -\boldsymbol{C}_m^T \boldsymbol{C}_n & \boldsymbol{0} & \boldsymbol{0} & \boldsymbol{0} \\ \boldsymbol{0} & -\boldsymbol{C}_m^T \boldsymbol{D}\boldsymbol{R}\boldsymbol{D}^T \boldsymbol{C}_n & \boldsymbol{0} & \boldsymbol{0} \end{bmatrix} \tag{15}$$

$$\boldsymbol{R} = \left(\boldsymbol{I} - \boldsymbol{D}^T\boldsymbol{D} \right)^{-1} \tag{16}$$

When the model presents many passivity violations, the solution of the frequency dependent eigenvalue problem (10) can be very challenging, since the number of purely imaginary eigenvalues can grow very large and the numerical conditioning may be poor. In this case, it is preferable to adopt a more robust technique based on an adaptive sampling of the singular values trajectories of the scattering matrix, aimed at the determination of the largest singular value exceeding one. The details of this procedure can be found in [30]. Both adaptive sampling and frequency-dependent Hamiltonian eigensolution are employed in different stages of our proposed passivity check and enforcement scheme, as discussed below.

V. Passivity enforcement

We illustrate our proposed passivity enforcement algorithms using a simplified scenario, depicted in Fig. 5. This plot depicts the trajectory of one singular value $\sigma_\nu(j\omega)$ of the model (8) exceeding the unit threshold in the bandwidth $(\tilde{\omega}_{2k-1}, \tilde{\omega}_{2k})$, thus causing a localized passivity violation. Model passivity is obtained by forcing this trajectory into the region below the unit threshold. In order to achieve this goal, several perturbation approaches are available, see [33], [37], [38], [39], [40], [41]. In this work, we concentrate on two different methods, both combined with a suitable optimality constraint for accuracy preservation, which are used in different stages of the proposed scheme. Some of the material that follows is not new. This section collects and presents in a systematic way preliminary results that were presented with less details in [37], [40], [41].

According to [36], where a similar notation was used in the context of GMoC-based transmission line macromodels, we denote these two schemes as *vertical* and *horizontal* displacement, respectively. Both schemes attempt at removing the passivity violation by applying a small perturbation to (8)

$$\boldsymbol{C}_m \leftarrow \boldsymbol{C}_m + \delta\boldsymbol{C}_m \,, \tag{17}$$

using a different form of local passivity constraints. The following two sections describe the two approaches.

A. Vertical displacement

The vertical displacement scheme for DRM's was first introduced in [37] and further developed in [40], [41]. In this scheme, we want to find a perturbation $\delta\hat{\sigma}_k$ such that

$$\hat{\sigma}_k + \delta\hat{\sigma}_k < 1\,, \tag{18}$$

where $\hat{\sigma}_k$ is the maximum value assumed by some σ_ν within a violation band. This perturbation is denoted with a vertical arrow in Fig. 5. Denoting the corresponding left and right singular vectors as $\boldsymbol{u}_k$ and $\boldsymbol{v}_k$, respectively, and performing a first-order singular value perturbation [49] on the model, we obtain

$$\delta\hat{\sigma}_k = \Re\left\{\sum_{m=1}^{M} \boldsymbol{u}_k^H \delta\boldsymbol{C}_m \boldsymbol{w}_{k,m}\right\} \tag{19}$$

where

$$\boldsymbol{w}_{k,m} = e^{-j\hat{\omega}_k\tau_m}\left(j\hat{\omega}_k\boldsymbol{I} - \boldsymbol{A}\right)^{-1}\boldsymbol{B}\boldsymbol{v}_k\,. \tag{20}$$

Using the properties of the Kronecker product [44] we obtain

$$\delta\hat{\sigma}_k = \sum_{m=1}^{M} \Re\left\{\boldsymbol{w}_{k,m}^T \otimes \boldsymbol{u}_k^H\right\}\mathrm{vec}(\delta\boldsymbol{C}_m)\,, \tag{21}$$

where the $\mathrm{vec}(\cdot)$ operator stacks the columns of its matrix argument in a single vector. There can be several constraints of this type, depending on the number of singular values that are being perturbed. We can collect all these constraints in a compact matrix form

$$\hat{\boldsymbol{\mathcal{Z}}}\,\mathrm{vec}(\delta\boldsymbol{\mathcal{C}}) \prec \hat{\boldsymbol{b}}\,, \tag{22}$$

where $\delta\boldsymbol{\mathcal{C}} = [\delta\boldsymbol{C}_1\ \cdots\ \delta\boldsymbol{C}_M]$,

$$\hat{\boldsymbol{\mathcal{Z}}} = \begin{bmatrix} \hat{\boldsymbol{Z}}_{1,1} & \cdots & \hat{\boldsymbol{Z}}_{1,M} \\ \vdots & \ddots & \vdots \\ \hat{\boldsymbol{Z}}_{K,1} & \cdots & \hat{\boldsymbol{Z}}_{K,M} \end{bmatrix}, \quad \hat{\boldsymbol{b}} = \begin{bmatrix} 1-\hat{\sigma}_1 \\ \vdots \\ 1-\hat{\sigma}_K \end{bmatrix}, \tag{23}$$

and

$$\hat{\boldsymbol{Z}}_{k,m} = \Re\left\{\boldsymbol{w}_{k,m}^T \otimes \boldsymbol{u}_k^H\right\}\,. \tag{24}$$

We denote (22) as *vertical passivity constraint*.

B. Horizontal displacement

The horizontal displacement scheme for DRM's was first introduced in [41]. In this section, we provide a more complete derivation and some implementation hints. Horizontal displacement aims at collapsing the passivity violation bands by perturbing their edges, as depicted by horizontal arrows in Fig. 5. Any of these edges $\tilde{s}_i = j\tilde{\omega}_i$ corresponds to a purely imaginary eigenvalue of (10). Therefore, this displacement is easily obtained by applying a suitable perturbation $\delta\boldsymbol{H}$ to the Hamiltonian matrix (11). The first-order relationship between this matrix and the corresponding eigenvalue perturbation reads [36]

$$j\tilde{\omega}_{i,p} - j\tilde{\omega}_i \simeq \frac{\boldsymbol{\xi}_i^H\boldsymbol{J}\delta\boldsymbol{H}\boldsymbol{\xi}_i}{\boldsymbol{\xi}_i^H\boldsymbol{J}(\boldsymbol{I}-\boldsymbol{H}'(\tilde{s}_i))\boldsymbol{\xi}_i} \tag{25}$$

where $\boldsymbol{\xi}_i$ is the eigenvector associated to $\tilde{s}_i$,

$$\boldsymbol{J} = \begin{bmatrix} \boldsymbol{0} & \boldsymbol{I} \\ -\boldsymbol{I} & \boldsymbol{0} \end{bmatrix}, \tag{26}$$

and $\boldsymbol{H}'(\tilde{s}_i)$ is the derivative of $\boldsymbol{H}(s)$ with respect to s, easily obtained from (11)

$$\begin{aligned}\boldsymbol{H}'(\tilde{s}_i) = &\sum_{m=1}^{M} \tau_m\left(\boldsymbol{\mathcal{W}}_m^+ e^{\tilde{s}_i\tau_m} - \boldsymbol{\mathcal{W}}_m^- e^{-\tilde{s}_i\tau_m}\right) \\ &+ \sum_{m,n=1}^{M}(\tau_m-\tau_n)\boldsymbol{\mathcal{W}}_{m,n}e^{\tilde{s}_i(\tau_m-\tau_n)}\,.\end{aligned} \tag{27}$$

The numerator in (25) can be evaluated as function of the perturbation matrices $\delta\boldsymbol{C}_m$. To this end, we introduce the four vectors

$$\begin{aligned}\boldsymbol{z}_{1,m,n}^T &= e^{\tilde{s}_i(\tau_n-\tau_m)}\boldsymbol{\xi}_{i,1}^H\boldsymbol{C}_n^T \\ \boldsymbol{z}_{2,m,n}^T &= e^{\tilde{s}_i(\tau_n-\tau_m)}\boldsymbol{\xi}_{i,2}^H\boldsymbol{C}_n^T\boldsymbol{D}\boldsymbol{R}\boldsymbol{D}^T \\ \boldsymbol{z}_{3,m}^T &= e^{-\tilde{s}_i\tau_m}\boldsymbol{\xi}_{i,3}^H\boldsymbol{B}\boldsymbol{R}\boldsymbol{D}^T \\ \boldsymbol{z}_{4,m}^T &= e^{-\tilde{s}_i\tau_m}\boldsymbol{\xi}_{i,4}^H\boldsymbol{B}\boldsymbol{R}\boldsymbol{D}^T\end{aligned} \tag{28}$$

where $\boldsymbol{\xi}_i^H = \begin{bmatrix}\boldsymbol{\xi}_{i,1}^H & \boldsymbol{\xi}_{i,2}^H & \boldsymbol{\xi}_{i,3}^H & \boldsymbol{\xi}_{i,4}^H\end{bmatrix}$, and we define

$$\begin{aligned}\tilde{\boldsymbol{Z}}_{i,m} = 2\Re\Bigg\{&\sum_{n=1}^{M}\left(\boldsymbol{\xi}_{i,1}^T\otimes\boldsymbol{z}_{1,m,n}^T + \boldsymbol{\xi}_{i,2}^T\otimes\boldsymbol{z}_{2,m,n}^T\right) \\ &+ \boldsymbol{\xi}_{i,2}^T\otimes\boldsymbol{z}_{3,m}^T + \boldsymbol{\xi}_{i,2}^T\otimes\boldsymbol{z}_{4,m}^T\Bigg\}\end{aligned} \tag{29}$$

If we collect all the terms $\tilde{\boldsymbol{Z}}_{i,m}$ in a matrix we can rewrite equations (25) as

$$\tilde{\boldsymbol{\mathcal{Z}}}\,\mathrm{vec}(\delta\boldsymbol{\mathcal{C}}) \simeq \tilde{\boldsymbol{b}} \tag{30}$$

where

$$\begin{aligned}\tilde{\boldsymbol{\mathcal{Z}}} &= \begin{bmatrix} \tilde{\boldsymbol{Z}}_{1,1} & \cdots & \tilde{\boldsymbol{Z}}_{1,M} \\ \vdots & \ddots & \vdots \\ \tilde{\boldsymbol{Z}}_{I,1} & \cdots & \tilde{\boldsymbol{Z}}_{I,M} \end{bmatrix}, \\ \tilde{\boldsymbol{b}} &= \begin{bmatrix} \Im\left\{\boldsymbol{\xi}_1^H\boldsymbol{J}\big(\boldsymbol{I}-\boldsymbol{H}'(\tilde{s}_1)\big)\boldsymbol{\xi}_1\right\}(\tilde{\omega}_{1,p}-\tilde{\omega}_1) \\ \vdots \\ \Im\left\{\boldsymbol{\xi}_I^H\boldsymbol{J}\big(\boldsymbol{I}-\boldsymbol{H}'(\tilde{s}_I)\big)\boldsymbol{\xi}_I\right\}(\tilde{\omega}_{I,p}-\tilde{\omega}_I) \end{bmatrix}.\end{aligned} \tag{31}$$

Expression (30) will be denoted as *horizontal passivity constraint*.

The amount of eigenvalue perturbation can be fine-tuned using a relaxation parameter α as

$$\tilde{\omega}_{i,p} - \tilde{\omega}_i = \begin{cases} \alpha(\tilde{\omega}_{i+1}-\tilde{\omega}_i) & \text{if } i = 2k-1, \\ \alpha(\tilde{\omega}_{i-1}-\tilde{\omega}_i) & \text{if } i = 2k. \end{cases} \tag{32}$$

A discussion on how to select α in the case of delayless macromodels is available in [29]. We adopt the same strategy in this work.

C. Accuracy preservation

Our proposed passivity compensation schemes amount to minimizing some norm $||\,\mathrm{vec}(\delta\boldsymbol{\mathcal{C}})||$ of the model perturbation while enforcing the constraints (22) or (30). This section details how to select the optimal norm by reporting results from our previous works [37], [40], [41]. This section is not new. We include it for completeness and to improve readability.

Algorithm 1 Passivity check and enforcement

Require: State space matrices $\boldsymbol{A}$, $\boldsymbol{B}$, $\boldsymbol{C}_m$, $\boldsymbol{D}$, $m = 1, \dots M$

$\mathcal{S} \leftarrow$ maximum singular values (adaptive sampling)
while $\mathcal{S} \neq \emptyset$ **do**
  Solve problem (42)
  $\boldsymbol{C}_m \leftarrow \boldsymbol{C}_m + \delta\boldsymbol{C}_m, \quad m = 1, \dots, M$
  $\mathcal{S} \leftarrow$ maximum singular values (adaptive sampling)
end while
$\mathcal{I} \leftarrow$ imaginary eigenvalues of (10)
while $\mathcal{I} \neq \emptyset$ **do**
  Solve problem (43)
  $\boldsymbol{C}_m \leftarrow \boldsymbol{C}_m + \delta\boldsymbol{C}_m, \quad m = 1, \dots, M$
  $\mathcal{I} \leftarrow$ imaginary eigenvalues of (10)
end while

In order to preserve the accuracy of the model, we minimize the energy of the induced perturbation on the impulse response

$$E = \sum_{p,q=1}^{P} \int_0^\infty |\delta h_{p,q}(t)|^2 \mathrm{d}t = \int_0^\infty \mathrm{tr}\left(\delta\boldsymbol{h}(t)\delta\boldsymbol{h}(t)^T\right) \mathrm{d}t \tag{33}$$

where

$$\delta\boldsymbol{h}(t) = \sum_{m=1}^{M} \delta\boldsymbol{C}_m e^{\boldsymbol{A}(t-\tau_m)}\boldsymbol{B}u(t-\tau_m)\,. \tag{34}$$

A direct substitution of (34) in (33) leads to

$$E = \mathrm{tr}\left(\sum_{m,n=1}^{M} \delta\boldsymbol{C}_m \boldsymbol{W}_{m,n} \delta\boldsymbol{C}_n^T\right) \tag{35}$$

with

$$\boldsymbol{W}_{m,n} = \int_{\max(\tau_m,\tau_n)}^\infty e^{\boldsymbol{A}(t-\tau_m)}\boldsymbol{B}\boldsymbol{B}^T e^{\boldsymbol{A}^T(t-\tau_n)}\mathrm{d}t\,. \tag{36}$$

Each of these integrals can be evaluated as the unique solution of the Lyapunov equation [47]

$$\boldsymbol{A}\boldsymbol{W}_{m,n} + \boldsymbol{W}_{m,n}\boldsymbol{A}^T + \boldsymbol{Q}_{m,n} = 0 \tag{37}$$

where

$$\boldsymbol{Q}_{m,n} = \begin{cases} e^{\boldsymbol{A}(\tau_n-\tau_m)}\boldsymbol{B}\boldsymbol{B}^T & \text{if } \tau_m < \tau_n\,, \\ \boldsymbol{B}\boldsymbol{B}^T & \text{if } \tau_m = \tau_n\,, \\ \boldsymbol{B}\boldsymbol{B}^T e^{\boldsymbol{A}^T(\tau_m-\tau_n)} & \text{if } \tau_m > \tau_n\,. \end{cases} \tag{38}$$

Collecting all these Lyapunov solutions in the block matrix

$$\boldsymbol{W} = \begin{bmatrix} \boldsymbol{W}_{1,1} & \cdots & \boldsymbol{W}_{1,M} \\ \vdots & \ddots & \vdots \\ \boldsymbol{W}_{M,1} & \cdots & \boldsymbol{W}_{M,M} \end{bmatrix}, \tag{39}$$

we can characterize the impulse perturbation energy as

$$\begin{aligned} E &= \mathrm{tr}(\delta\boldsymbol{\mathcal{C}}\boldsymbol{W}\delta\boldsymbol{\mathcal{C}}^T) = \mathrm{tr}(\delta\boldsymbol{\mathcal{C}}\boldsymbol{K}^T\boldsymbol{K}\delta\boldsymbol{\mathcal{C}}) \\ &= \mathrm{tr}(\delta\boldsymbol{\mathcal{C}}_{\boldsymbol{K}}\delta\boldsymbol{\mathcal{C}}_{\boldsymbol{K}}^T) = \|\,\mathrm{vec}(\delta\boldsymbol{\mathcal{C}}_{\boldsymbol{K}})\|^2\,, \end{aligned} \tag{40}$$

where the Cholesky decomposition $\boldsymbol{W} = \boldsymbol{K}^T\boldsymbol{K}$ is used. This characterization shows that the minimal perturbation in the model response is achieved by minimizing a weighted norm of $\delta\boldsymbol{\mathcal{C}}$. In our implementation, this weight is simply applied as a basis change defined by the Cholesky factor $\boldsymbol{K}$

$$\mathrm{vec}(\delta\boldsymbol{\mathcal{C}}) = \mathrm{vec}(\boldsymbol{K}^{-1}\delta\boldsymbol{\mathcal{C}}_{\boldsymbol{K}}) = (\boldsymbol{I}\otimes\boldsymbol{K}^{-1})\,\mathrm{vec}(\delta\boldsymbol{\mathcal{C}}_{\boldsymbol{K}})\,. \tag{41}$$

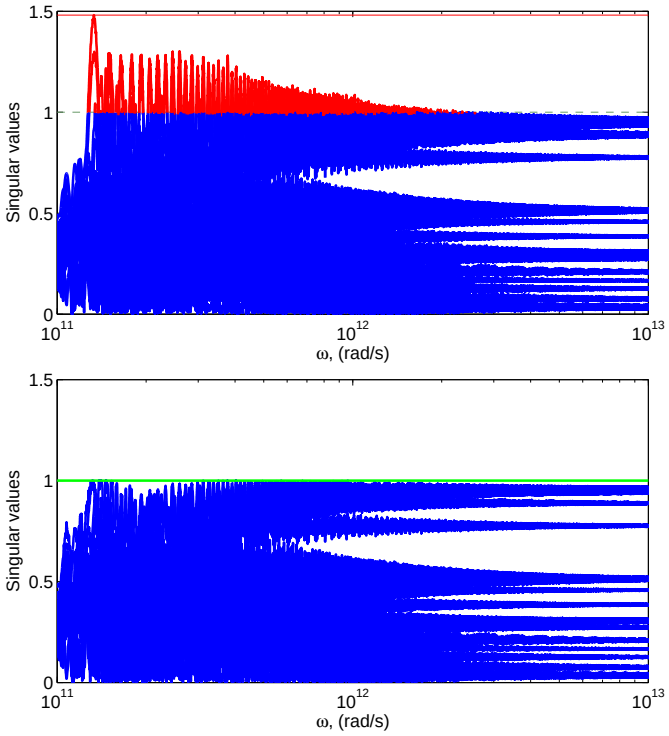

Fig. 6. Singular values trajectories before and after passivity enforcement for the case 1.

In summary, we formulate our proposed passivity enforcement as

$$\begin{aligned} \text{minimize} \quad & \|\,\mathrm{vec}(\delta\boldsymbol{\mathcal{C}}_{\boldsymbol{K}})\| \\ \text{s.t.} \quad & \hat{\boldsymbol{\mathcal{Z}}}(\boldsymbol{I}\otimes\boldsymbol{K}^{-1})\,\mathrm{vec}(\delta\boldsymbol{\mathcal{C}}_{\boldsymbol{K}}) \prec \hat{\boldsymbol{b}} \end{aligned} \tag{42}$$

for the vertical displacement algorithm and

$$\begin{aligned} \text{minimize} \quad & \|\,\mathrm{vec}(\delta\boldsymbol{\mathcal{C}}_{\boldsymbol{K}})\| \\ \text{s.t.} \quad & \tilde{\boldsymbol{\mathcal{Z}}}(\boldsymbol{I}\otimes\boldsymbol{K}^{-1})\,\mathrm{vec}(\delta\boldsymbol{\mathcal{C}}_{\boldsymbol{K}}) = \tilde{\boldsymbol{b}} \end{aligned} \tag{43}$$

for the horizontal displacement algorithm. Problem (43) is solved using standard pseudoinverse methods, whereas (42) is solved using an interior-point convex optimization method [48].

D. Global passivity enforcement

Global passivity enforcement is achieved by iterative application of the optimal vertical and horizontal perturbation schemes (42) and (43). Our implementation choices, detailed in Algorithm 1, are best described through an example (case 1 in Section VI). The top panel of Fig. 6 depicts the singular value trajectories of an 18-port channel model. The portion of these curves that exceeds the unit threshold is highlighted in red color. As the figure demonstrates, the singular values are characterized by a strong oscillatory behavior, due to the frequency dependence of the various delay terms in (1), which extends well beyond the modeling bandwidth (in this case

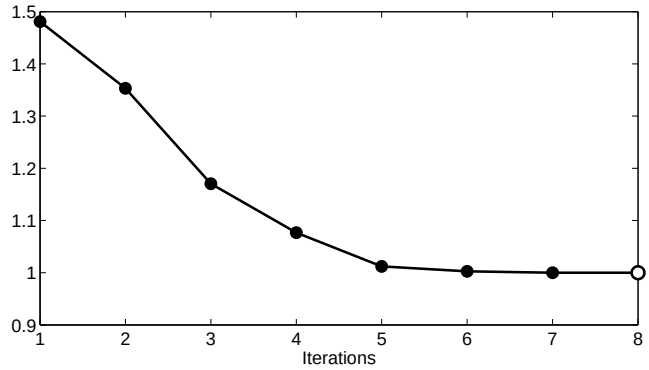

Fig. 7. Convergence of passivity enforcement algorithm for the case 1.

TABLE II
MAIN PARAMETERS OF THE TEST CASES

Case	No. of ports	No. of samples	Bandwidth
1	18	1024	20 GHz
2	18	1024	20 GHz
3	18	2043	10 GHz
4	18	1024	20 GHz

20 GHz). Due to these oscillations, the number of crossings of the unit threshold is very large, making the direct solution of the frequency-dependent eigenvalue problem (10) impractical.

The global passivity enforcement scheme is thus started in step 1 with an adaptive sampling [30] aimed at the identification of the maximum singular value, followed by iterative application of the vertical perturbation (steps 2–6), until no singular values larger than one are found. At this point, it is expected that a very limited number of crossings, if any, is present. Therefore, we proceed in step 7 to the computation of the imaginary eigenvalues of (10). The horizontal perturbation is then applied iteratively (steps 8–12) until no imaginary eigenvalues are detected. At the end of this loop model is passive.

Figure 7 reports the evolution of the maximum singular value through the iterations for the same test case of Fig. 6. The first seven iterations were performed by the vertical scheme, and only in the last iteration the eigenvalue problem (10) and the horizontal displacement algorithm were applied. The bottom plot of Fig. 6 reports the singular values of the model after the last iteration, which are uniformly below the unit threshold, as expected.

VI. RESULTS

In this section, the proposed macromodeling flow is applied to a large set of cases of practical interest. The structures under investigation are depicted in Fig. 8, whereas Table II lists the main features of the associated data. All these structures correspond to a single victim path surrounded by eight aggressors, resulting in 18 electrical ports. The raw scattering responses were derived by cascading scattering responses of individual substructures forming the channels, which in turn were obtained from 2D and/or 3D field solvers. An example of model extraction from measured data will be presented in Section VI-C.

Case 1: node to IO card channel

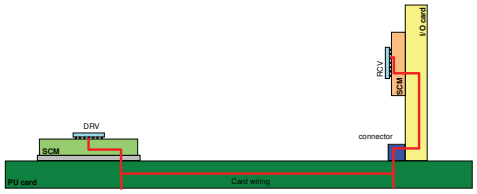

Case 2: node to node channel across backplane

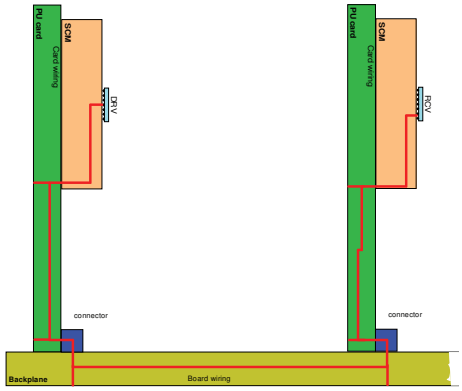

Case 3: node to node channel across flexfoil

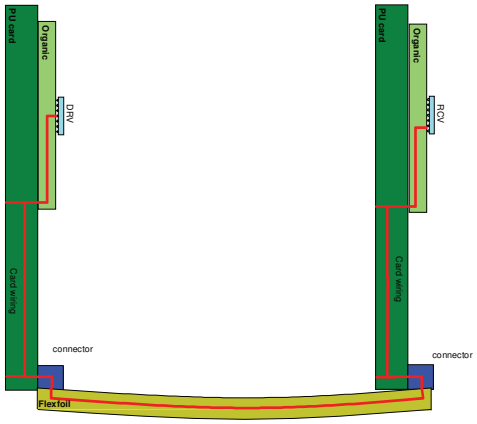

Case 4: on-node channel

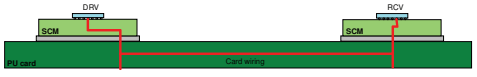

Fig. 8. Graphical representations of the structures under investigation.

TABLE III
IDENTIFICATION RESULTS

Case	RMS Error $\times 10^{-3}$	CPU time (s)
1	5.76	276.54
2	16.18	377.42
3	7.42	87.40
4	5.07	166.51

TABLE IV
PASSIVITY ENFORCEMENT RESULTS

Case	$\hat{\sigma}$	$\hat{f}$, GHz	$\varepsilon_1 \times 10^{-3}$	$\varepsilon_2 \times 10^{-3}$	CPU time (s)
1	-	-	-	-	-
2	1.4662	21.13	17.57	23.89	352.40
3	1.3330	14.96	7.28	10.39	322.23
4	1.6109	26.00	19.14	19.80	656.04

A. Model identification and passivity enforcement

The frequency samples of each structure have been processed by the I-DVF algorithm of Section III, resulting in an initial DRM. The accuracy of all models expressed as worst-case RMS error and the CPU times needed for the identification are reported in Table III.

A passivity check reveals that all models suffer from passivity violations outside the modeling bandwidth, with the exception of Case 1 which is already passive after the identification process. After application of Algorithm 1, passivity was achieved for all cases in a variable number of iterations, ranging from 6 to 10. A summary of the main results is provided in Table IV, in particular the maximum singular value $\hat{\sigma}$ before passivity enforcement and its corresponding frequency $\hat{f}$, the RMS error between original model and the passive model ε_1, the RMS error between raw data and the passive model ε_2, and the CPU time required by the algorithm. We remark that a consistent portion (about 90%) of the CPU times is used for the passivity check. The perturbation stages (42) and (43) are very efficient, since they require the solution of a small-size standard quadratic problem with linear constraints, for which very efficient solvers are available, as we have seen in Section V.

Figures 9–12 demonstrate the accuracy of the passive models for several scattering matrix entries. In particular, for each test case we consider three scattering parameters (a reflection, a transmission and a cross-talk). All diagrams show an excellent match between original data and passive models.

B. Transient simulations

The passive macromodels documented in the foregoing section were synthesized into SPICE-compatible netlists for transient analysis and channel qualification. For this task, we used the IBM PowerSpice solver. This solver (as well as most leading commercial solvers) allows, in addition to standard circuit elements, a library of controlled sources in "Laplace" form. These elements are specified to the solver in terms of poles and residues, i.e., they match exactly the Delay-Rational Macromodel form (1). Also ideal delay elements are available as special controlled sources. Therefore, the netlist synthesis of our macromodels is straightforward. If Laplace and delay sources are not available with the adopted SPICE solver, it is possible to use a less specialized and more general synthesis as documented in [23].

Most channel qualifications are performed through eye diagrams. So, we computed eye diagrams for each of the four channels, with different termination schemes and simulation settings. In all cases, a pseudorandom bit sequence with 1000 bits was applied to port 9, corresponding to the center victim channel in each bus. The bit rate was 2Gbps in all cases, except for Case 3, for which we used a 1Gbps excitation. The eye diagram was then computed at the receiver input, i.e., port 10. All results that will be labeled with "Single" correspond to a 2-port model consisting of the active channel alone, with all other ports removed. Conversely, all results labeled with "Coupled" correspond to the full 18-port macromodel, thus including also 8 aggressor channels in addition to the victim channel. When present, all aggressor channels were excited by identical synchronous clock signals at the same bit rate of the active driver.

Two different termination schemes were used, in order to compare eye diagram results and CPU time. All results that will be labeled with "LIN" were obtained with linear Thevenin drivers with 40Ω internal resistance. All results labeled with "NL" were instead computed by using suitable nonlinear and dynamic macromodels of the MπLog class [52] for all driving sources (both active driver and aggressors). In particular, the precompensated driver models documented in [53] were adopted. Such drivers are able to adapt their output impedance to the history of the bits being transmitted, thus achieving effective precompensation and improving transmission quality (eye opening). More precisely, the adopted driver maintains its output impedance to 40Ω during non-switching sequences, and lowers the impedance to 20Ω when switching occurs. Linear receivers consisting of identical pull-up and pull-down loads (100 Ω resistors in parallel with 1 pF capacitors, with 1.1 V bias voltage) were used in all cases.

Individual eye diagrams are collected in Figures 13–16. The eye degradation due to the presence of aggressors is evident (top panels vs bottom panels in each figure). The eye quality improvement due to the precompensated drivers is also clearly visible (left panels vs right panels in each figure).

Finally, we report the total simulation time required by each simulation in Table V. These results show that individual channel simulation requires minimal CPU time (few seconds) when linear terminations are used. When nonlinear models are used, there is some additional overhead due to the internal complexity of the driver models (5–10 times slower), and the total CPU time is dominated by the nonlinear driver models. In any case, a 1000-bit eye is computed in less than one minute. The fully coupled simulations, including aggressor signals, require more CPU time. The linear termination cases require about 20 minutes on average, whereas the nonlinear termination cases run in 40–60 minutes. This performance is quite acceptable, given that our proposed technique includes full and arbitrary nonlinearities of termination networks. Overall, these results demonstrate the feasibility of our macromodeling approach, that is able to deliver fast and accurate channel qualification results via simple circuit-based simulation.

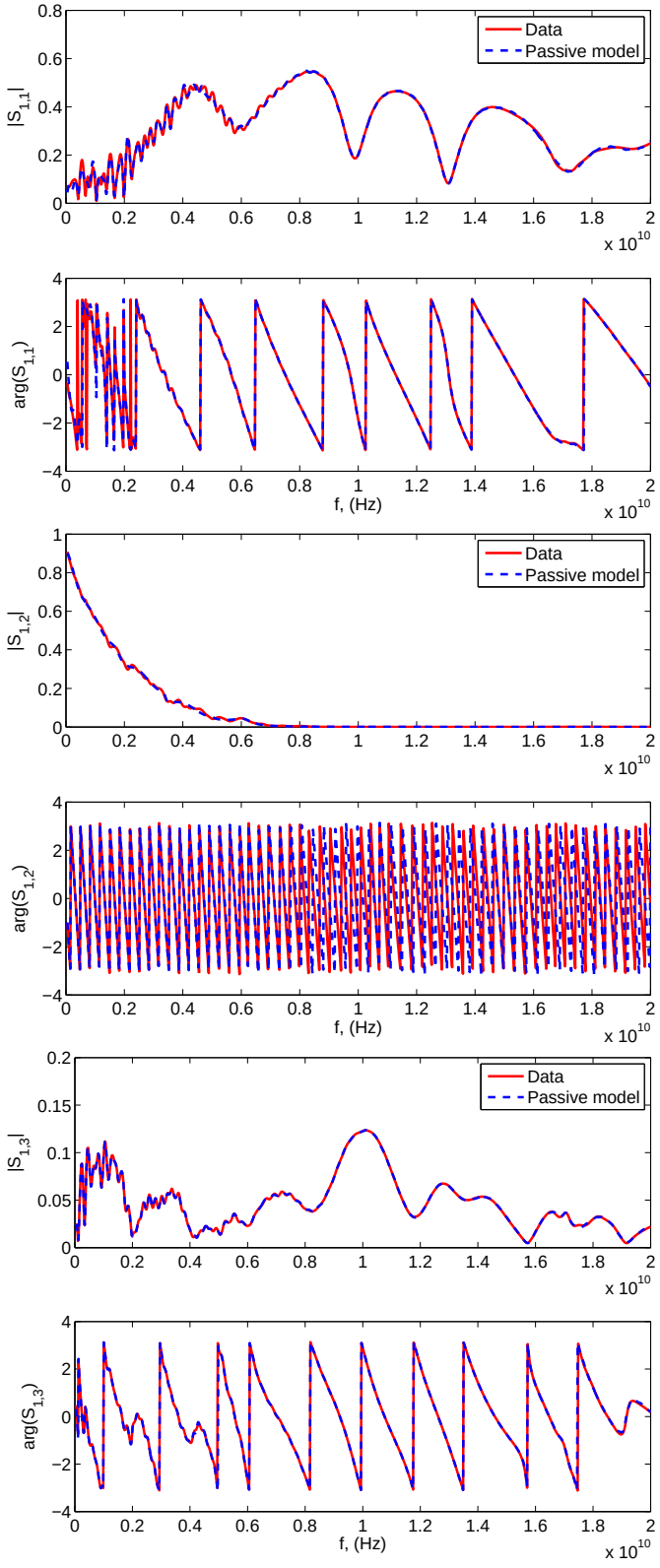

Fig. 9. Comparisons between the original data and passive model for the test case 1.

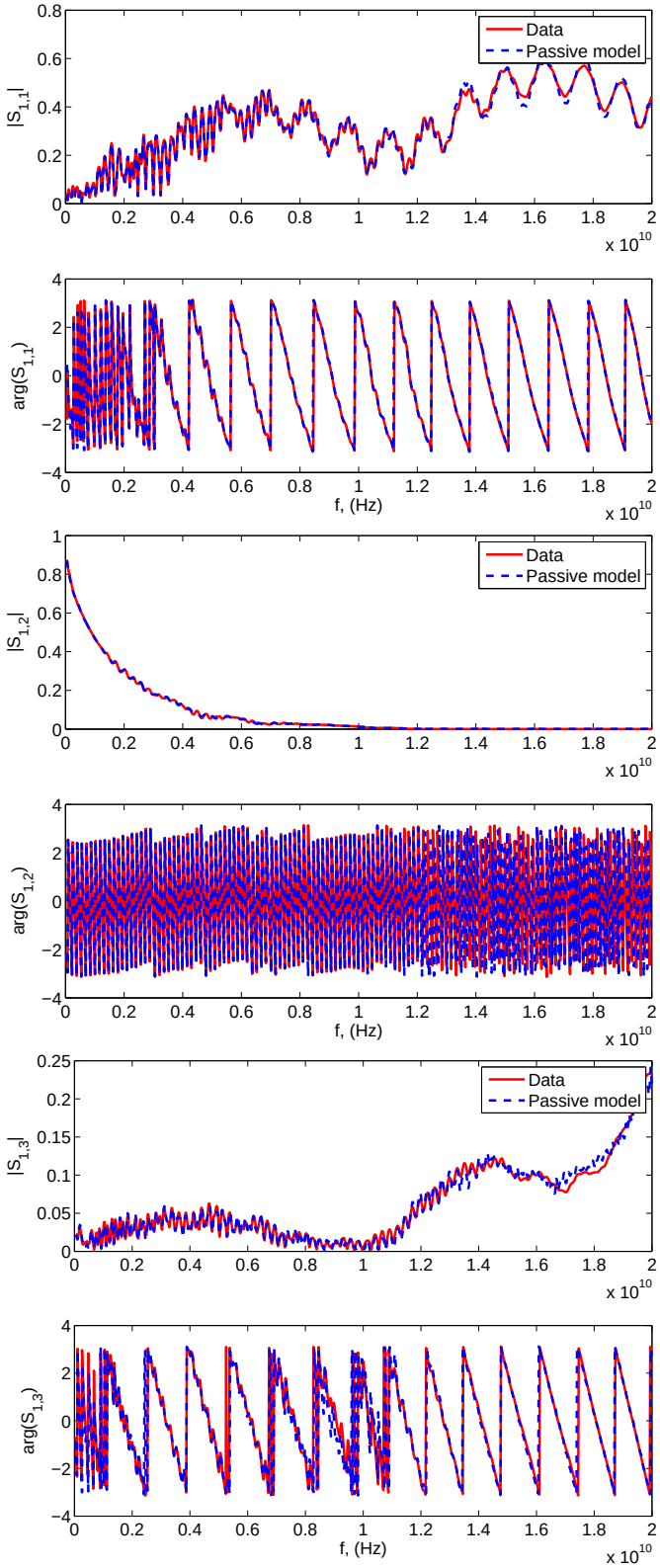

Fig. 10. As in Fig. 9, but for the test case 2.

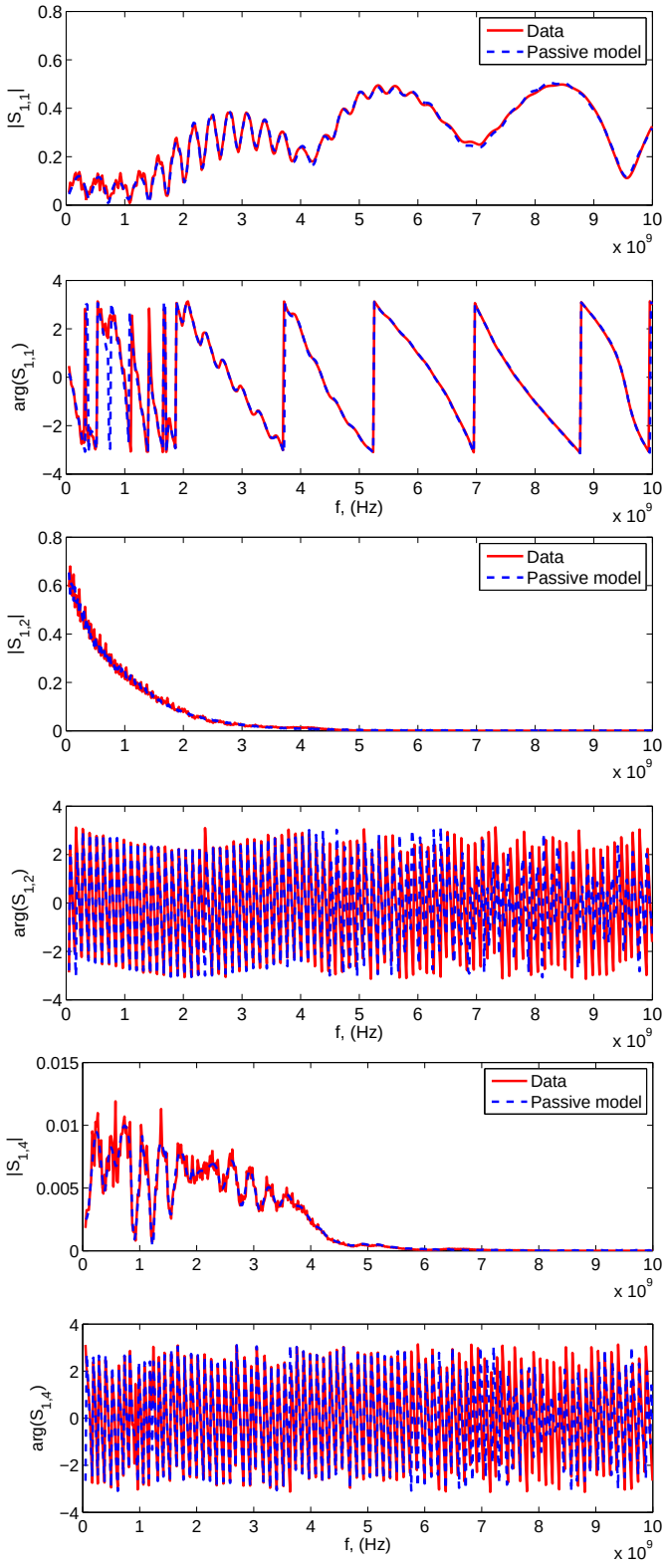

Fig. 11. As in Fig. 9, but for the test case 3.

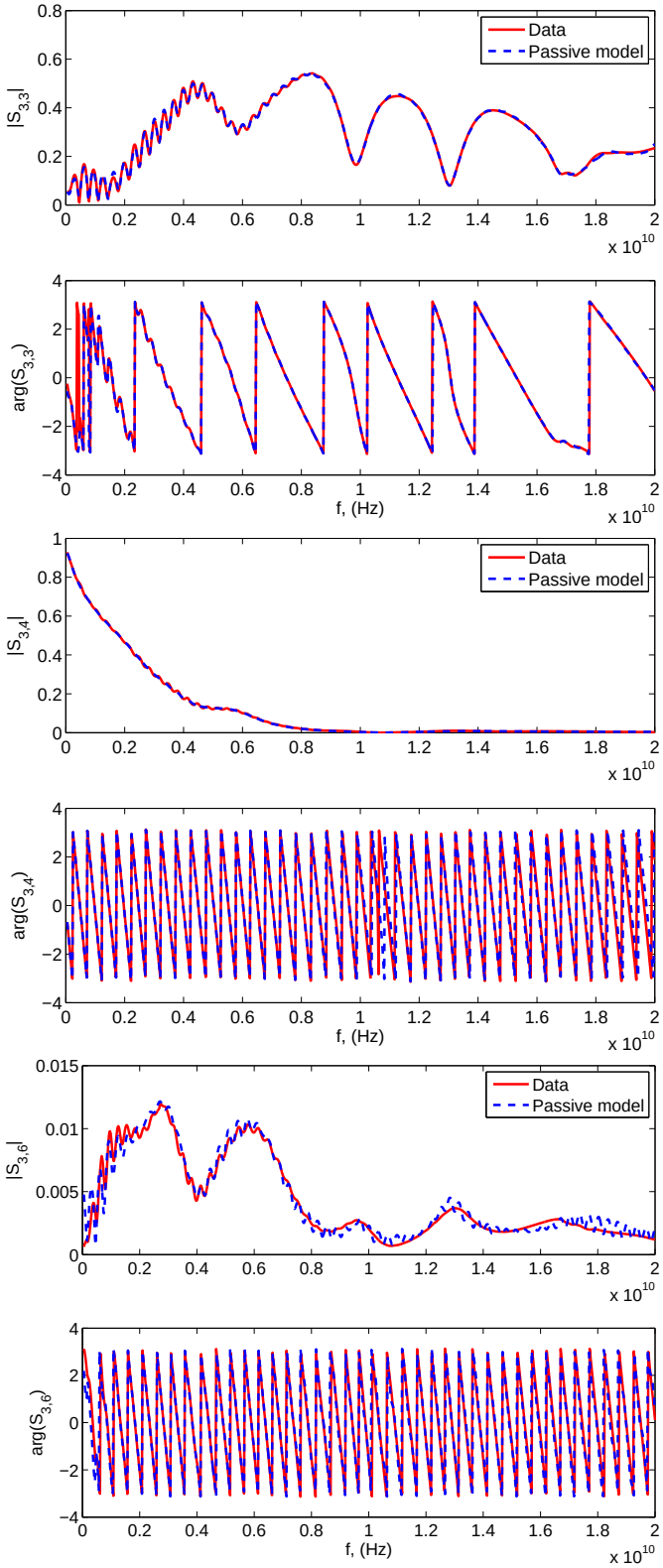

Fig. 12. As in Fig. 9, but for the test case 4.

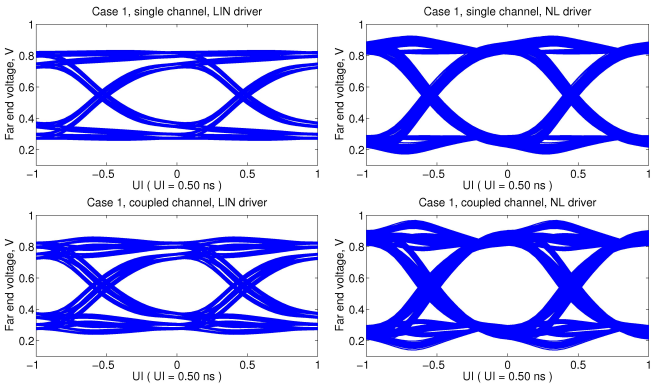

Fig. 13. Comparison of eye diagrams (1000 bits) at 2Gbps for Case 1.

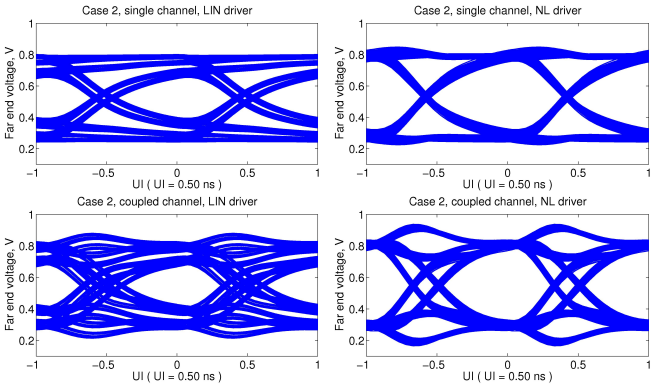

Fig. 14. Comparison of eye diagrams (1000 bits) at 2Gbps for Case 2.

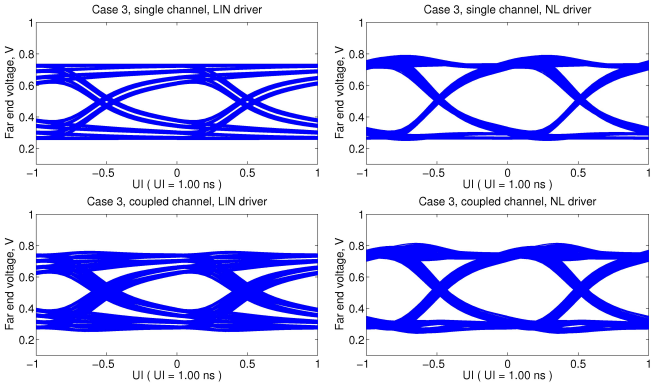

Fig. 15. Comparison of eye diagrams (1000 bits) at 1Gbps for Case 3.

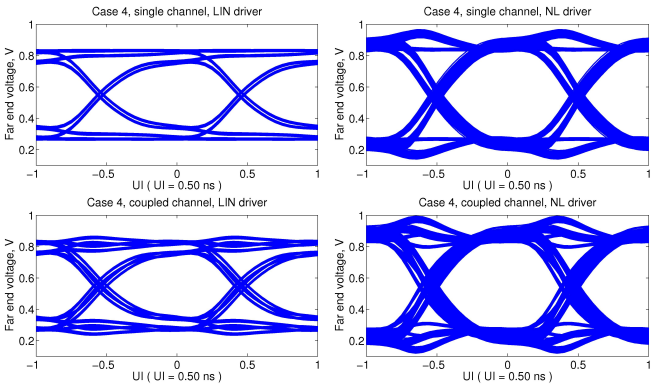

Fig. 16. Comparison of eye diagrams (1000 bits) at 2Gbps for Case 4.

TABLE V

TOTAL SIMULATION TIME REQUIRED BY POWERSPICE FOR THE COMPUTATION OF 1000-BIT EYE DIAGRAMS. 'SINGLE' AND 'COUPLED' DENOTE ACTIVE CHANNEL ONLY AND FULLY-COUPLED CHANNEL WITH AGGRESSORS, RESPECTIVELY. 'LIN' AND 'NL' INDICATE THAT LINEAR AND NONLINEAR MODELS WERE USED FOR DRIVERS/RECEIVERS.

Case	Single LIN	Single NL	Coupled LIN	Coupled NL
1	9s	51s	21m 45s	53m 34s
2	10s	53s	18m 9s	41m 58s
3	7s	53s	22m 55s	61m 54s
4	4s	47s	24m 20s	52m 13s

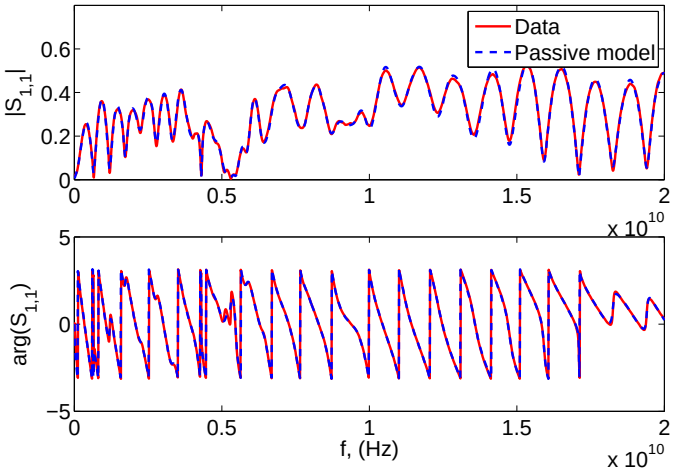

Fig. 17. Comparisons between the original (measured) data and passive model for the channel of Section VI-C.

C. Macromodel extraction from measured data

This last section documents an application example with measured data. A long channel connecting a processing card to an I/O card through a midplane was characterized using a 4-port VNA measurement up to 20 GHz. The structure includes two card-midplane connectors with the associated via fields, plus various discontinuities at the package-board, package, and chip-package levels. We report this example since direct measurements, when available, are guaranteed to include all possible lumped and distributed electromagnetic interactions.

The proposed I-DVF scheme followed by global passivity enforcement was applied, obtaining the results depicted in Fig. 17. The plot compares one of the scattering responses of the identified passive model with measured data. No significant difference can be noted. A similar accuracy was achieved also for the other scattering responses, for which the maximum RMS model vs data error resulted 17.9×10^{-3}. This accuracy is comparable to the other cases reported in Table III. This example demonstrates applicability of the proposed model extraction flow also to direct measurements, thus indirectly proving that the DRM model structure (1) is indeed appropriate for general electrically long channels.

ACKNOWLEDGEMENT

This work was supported in part by Istituto Superiore "Mario Boella", Torino, Italy, and in part by the Italian Ministry of University (MIUR) under a Program for the

Development of Research of National Interest (PRIN grant #2008W5P2K).

REFERENCES

[1] R. Achar and M. Nakhla, "Simulation of high-speed interconnects," *Proceedings of the IEEE*, vol. 89, no. 5, pp. 693–728, May 2001.

[2] C. Paul, *Analysis of Multiconductor Transmission Lines*. John Wiley & Sons, Inc. New York, NY, USA, 1994.

[3] A. Deutsch, "Electrical characteristics of interconnections for high-performance systems," *Proceedings of the IEEE*, vol. 86, no. 2, pp. 315–357, 1998.

[4] Beyene, W.T.; "Applications of Multilinear and Waveform Relaxation Methods for Efficient Simulation of Interconnect-Dominated Nonlinear Networks," *Advanced Packaging, IEEE Transactions on*, vol. 31, no. 3, pp. 637–648, Aug. 2008.

[5] Beyene, W.T.; Madden, C.; Jung-Hoon Chun; Haechang Lee; Frans, Y.; Leibowitz, B.; Ken Chang; Namhoon Kim; Ting Wu; Yip, G.; Perego, R.; "Advanced Modeling and Accurate Characterization of a 16 Gb/s Memory Interface," *Advanced Packaging, IEEE Transactions on*, vol. 32, no. 2, pp. 306–327, May 2009.

[6] Balamurugan, G.; Casper, B.; Jaussi, J.E.; Mansuri, M.; O'Mahony, F.; Kennedy, J.; "Modeling and Analysis of High-Speed I/O Links," *Advanced Packaging, IEEE Transactions on*, vol. 32, no. 2, pp. 237–247, May 2009.

[7] Sanders, A.; "Statistical Simulation of Physical Transmission Media," *Advanced Packaging, IEEE Transactions on*, vol. 32, no. 2, pp. 260–267, May 2009.

[8] B. Gustavsen, A. Semlyen, "Rational approximation of frequency responses by vector fitting", *IEEE Trans. Power Delivery*, Vol. 14, N. 3, July 1999, pp. 1052–1061.

[9] B. Gustavsen, A. Semlyen, "A robust approach for system identification in the frequency domain", *IEEE Trans. Power Delivery*, Vol. 19, N. 3, July 2004, pp. 1167–1173.

[10] D. Deschrijver, B. Haegeman, T. Dhaene, "Orthonormal Vector Fitting: A Robust Macromodeling Tool for Rational Approximation of Frequency Domain Responses", *IEEE Trans. Adv. Packaging*, vol. 30, pp. 216–225, May 2007.

[11] S. Grivet-Talocia, M. Bandinu, "Improving the Convergence of Vector Fitting in Presence of Noise", *IEEE Transactions on Electromagnetic Compatibility*, vol. 48, n. 1, pp. 104-120, February, 2006.

[12] W.Beyene, J. Schutt-Ainé, "Accurate Frequency-Domain Modeling and Efficient Circuit Simulation of High-Speed Packaging Interconnects", *IEEE Trans. Microwave Theory Tech.*, vol. 45, pp. 1941-1947, Oct. 1997

[13] K. L. Choi, M. Swaminathan, "Development of Model Libraries for Embedded Passives Using Network synthesis", *IEEE Trans. Circuits and Systems II*. vol. 47, pp. 249–260, Apr. 2000.

[14] M. Elzinga, K. Virga, L. Zhao, J. L. Prince, "Pole-Residue Formulation for transient simulation of high-frequency interconnects using Householder LS curve-fitting techniques", *IEEE Trans. Comp. Packag. Manufact. Technol.*, vol. 23, pp. 142–147, Mar. 2000

[15] M. Elzinga, K. Virga, J. L. Prince, "Improve Global Rational Approximation Macromodeling Algorithm for Networks Characterized by Frequency-Sampled Data", *IEEE Trans. Microwave Theory Tech.*, vol. 48, pp. 1461–1467, Sept. 2000

[16] S. Lin and E. S. Kuh, "Transient simulation of lossy interconnects based on the recursive convolution formulation," *IEEE Trans. Circuits Systems I*, vol. 39, pp. 879-892, Nov. 1992.

[17] J. Morsey, A. C. Cangellaris, "PRIME: Passive Realization of Interconnects Models from Measures Data", in *Proc. IEEE* 10^{th} *Topical Meeting on Electr. Perf. of Electron. Packag.*, 2001, pp. 47–50.

[18] S. Grivet-Talocia, H. M. Huang, A. E. Ruehli, F. Canavero, I. M. Elfadel, "Transient Analysis of Lossy Transmission Lines: an Effective Approach Based on the Method of Characteristics," *IEEE Trans. Advanced Packaging*, pp. 45–56, vol. 27, n. 1, Feb. 2004.

[19] S. Grivet-Talocia, "Delay-based macromodels for long interconnects via time-frequency decompositions," in *IEEE* 15^{th} *Topical Meeting on Electrical Performance of Electronic Packaging, Scottsdale, Arizona*, pp. 199–202, Oct. 23–25, 2006.

[20] A. Charest, D. Saraswat, M. Nakhla, R. Achar, N. Soveiko, "Compact Macromodeling of High-Speed Circuits via Delayed Rational Functions," *IEEE Microwave and Wireless Components Letters* Vol. 17, No. 12, pp. 828–830, Dec. 2007.

[21] A. Chinea, P. Triverio, and S. Grivet-Talocia, "Compact macromodeling of electrically long interconnects," in *IEEE* 17^{th} *Topical Meeting on Electrical Performance of Electronic Packaging (EPEP 2008), San Jose, CA*, pp. 199–202, Oct. 27–29, 2008.

[22] A. Charest, M. Nakhla, R. Achar, "Delay Extracted Stable Rational Approximations for Tabulated Networks With Periodic Reflections," *IEEE Microwave and Wireless Components Letters*, Vol. 19, No. 12, Dec 2009, pp. 768–770.

[23] A. Chinea, P. Triverio, S. Grivet-Talocia, "Delay-Based Macromodeling of Long Interconnects from Frequency-Domain Terminal Responses," *IEEE Transactions on Advanced Packaging*, Vol. 33, No. 1, pp. 246–256, Feb. 2010.

[24] P. Triverio, S. Grivet-Talocia, A. Chinea, "Identification of highly efficient delay-rational macromodels of long interconnects from tabulated frequency data," *IEEE Transactions on Microwave Theory and Techniques*, vol. 58, no. 3, pp. 566–577, 2010.

[25] A. Charest, M. Nakhla, R. Achar, D. Saraswat, N. Soveiko, I. Erdin, "Time Domain Delay Extraction-Based Macromodeling Algorithm for Long-Delay Networks," *IEEE Transactions on Advanced Packaging*, Vol. 33, No. 1, pp. 219–235, Feb. 2010.

[26] D. B. Kuznetsov and J. E. Schutt-Ainé, "Optimal transient simulation of transmission lines," *IEEE Trans. Circuits Systems I*, vol. 43, pp. 110-121, Feb. 1996.

[27] P. Triverio, S. Grivet-Talocia, M. S. Nakhla, F. Canavero, R. Achar, "Stability, Causality, and Passivity in Electrical Interconnect Models," *IEEE Transactions on Advanced Packaging*, Vol. 30, No. 4, pp. 795–808, Nov. 2007.

[28] S. Grivet-Talocia, "On Driving Non-passive Macromodels to Instability," *International Journal of Circuit Theory and Applications*, Vol. 37, No. 8, pp. 863–886, Oct. 2009.

[29] S. Grivet-Talocia, "Passivity enforcement via perturbation of Hamiltonian matrices," *IEEE Transactions CAS-I*, Vol. 51, No. 9, pp. 1755–1769, Sept. 2004

[30] S. Grivet-Talocia, "An Adaptive Sampling Technique for Passivity Characterization and Enforcement of Large Interconnect Macromodels," *IEEE Transactions on Advanced Packaging*, Vol. 30, No. 2, May 2007, pp. 226–237.

[31] B. Gustavsen, J. Nordstrom, "Pole Identification for The Universal Line Model Based on Trace Fitting," *IEEE Transactions on Power Delivery*, Vol. 23, No. 1, pp. 472–479, Jan. 2008.

[32] B. Gustavsen, "Time delay identification for transmission line modeling," in *Proc. 8th IEEE Workshop Signal Propagation Interconnects, Heidelberg, Germany*, May 9–12, 2004, pp. 103–106.

[33] A. Charest, M. Nakhla, R. Achar, "Scattering Domain Passivity Verification and Enforcement of Delayed Rational Functions," *IEEE Microwave and Wireless Components Letters*, Vol. 19, No. 10, Oct. 2009, pp. 605–607.

[34] A. Charest, M. Nakhla, R. Achar, "Efficient Passivity Verification of Delayed Rational Function Macromodels from Networks Characterized by Tabulated Data," in *14th IEEE Workshop on Signal Propagation on Interconnects, Hildesheim, Germany*, pp. 109//112, May 9–12, 2010.

[35] E. Gad, C. Chen, M. Nakhla, R. Achar, "Passivity Verification in Delay-Based Macromodels of Electrical Interconnects," *IEEE Trans. CAS-I*, Vol. 52, No. 10, Oct. 2005, pp. 2173–2187.

[36] A. Chinea, S. Grivet-Talocia, "Perturbation Schemes for Passivity Enforcement of Delay-Based Transmission Line Macromodels," *IEEE Transactions on Advanced Packaging*, Vol. 31, No. 3, pp. 568-578, Aug. 2008

[37] A. Chinea, S. Grivet-Talocia, P. Triverio, "On the performance of weighting schemes for passivity enforcement of delayed rational macromodels of long interconnects," in *IEEE* 18^{th} *Conference on Electrical Performance of Electronic Packaging and Systems (EPEPS 2009)*, Portland (Tigard), Oregon, Oct. 19–21, 2009.

[38] A. Charest, M. Nakhla, R Achar, C. Chen, "Passivity verification and enforcement of delayed rational function macromodels from networks characterized by tabulated data," in *IEEE Workshop on Signal Propagation on Interconnects, 2009. SPI'09*, pp. 1–4, May 12–15, 2009.

[39] A. Charest, M. Nakhla, R Achar, "Passivity verification and enforcement of delayed rational approximations from scattering parameter based tabulated data," in *IEEE* 18^{th} *Conference on Electrical Performance of Electronic Packaging and Systems (EPEPS 2009)*, Portland (Tigard), Oregon, Oct. 19–21, 2009, pp. 65–68.

[40] A. Chinea, S. Grivet-Talocia, D. Deschrijver, T. Dhaene, L. Knockaert, "On the construction of guaranteed passive macromodels for high-speed channels," *Design, Automation and Test in Europe (DATE 10)*, Dresden (Germany), pp. 1142-1147, March 8-12, 2010.

[41] A. Chinea, P. Triverio, and S. Grivet-Talocia, "Passive delay-based macromodels for signal integrity verification of multi-chip links," in *14th IEEE Workshop on Signal Propagation on Interconnects, Hildesheim, Germany*, pp. 1–4, May 9–12, 2010.

[42] N. Nakhla, M. Nakhla, R. Achar, "Simplified Delay Extraction-Based Passive Transmission Line Macromodeling Algorithm," *IEEE Transactions on Advanced Packaging*, Vol. 33, No. 2, May 2010, pp. 498–509.

[43] J. A. Nelder and R. Mead, "A simplex method for function minimization," *Computer Journal*, Vol. 7, pp. 308–313, 1965

[44] C. F. Van Loan, "The ubiquitous Kronecker product" *J. Comput. Appl. Math.*, Vol. 123, 2000, pp. 85–100.

[45] D. H. Griffel, *Applied Functional Analysis*, John Wiley & Sons, 1984.

[46] E. O. Brigham, *The fast Fourier transform and its applications*, Englewood Cliffs: Prentice- Hall, 1988.

[47] K. Zhou, J. Doyle, and K. Glover, *Robust and optimal control*. Prentice-Hall, 1996.

[48] Stephen Boyd, Lieven Vandenberghe, *Convex Optimization*, Cambridge University Press, 2004.

[49] J. H. Wilkinson, *The algebraic eigenvalue problem*, Oxford University Press, London, 1965.

[50] "Touchstone® File Format Specification, Version 2.0," available online: `http://www.eda.org/ibis/home/specs/specs.htm`

[51] LTSPICE IV, *Linear Technology*, available online: `www.linear.com`

[52] I.S.Stievano, I.A.Maio, F.G.Canavero, "M[pi]log, Macromodeling via Parametric Identification of Logic Gates," *IEEE Transactions on Advanced Packaging*, Vol. 27, No. 1, pp. 15–23, Feb. 2004.

[53] Cocchini, M; Becker, W.D.; Katopis, G.; Pytel, S.G.; "Time-domain simulation of system interconnect using convolution and Newton-Raphson iteration methods," *Proc. 60th Electronic Components and Technology Conference (ECTC), Las Vegas, NV, USA*, 1–4 June 2010, pp. 646–651.

Alessandro Chinea the Laurea Specialistica (M.Sc.) and Ph.D. degrees in electronic engineering from Politecnico di Torino, Italy in 2006 and 2010, respectively. Since 2007, he joined the EMC group where he is currently a research assistant. In 2009 he spent a period at the Department of Information Technology (INTEC) of the Ghent University, Belgium, working under the supervision of the professors T. Dhaene and L. Knockaert. His research interests concern macromodeling of electrical interconnects for electromagnetic compatibility and signal integrity problems. In particular, he works on algorithms development for passivity check and enforcement of lumped and distributed models. Mr. Chinea received the Optime Award from the Unione Industriale di Torino and he was selected for the IBM EMEA Best Student Recognition Event 2006.

Stefano Grivet-Talocia (M'98–SM'07) received the Laurea and the Ph.D. degrees in electronic engineering from Politecnico di Torino, Italy. From 1994 to 1996, he was with the NASA/Goddard Space Flight Center, Greenbelt, MD, USA. Currently, he is an Associate Professor of Circuit Theory with Politecnico di Torino. His research interests are in passive macromodeling of lumped and distributed interconnect structures, modeling and simulation of fields, circuits, and their interaction, wavelets, time-frequency transforms, and their applications. He is author of more than 120 journal and conference papers. He is co-recipient of the 2007 Best Paper Award of the IEEE Trans. Advanced Packaging. He received the IBM Shared University Research (SUR) Award in 2007, 2008 and 2009. Dr. Grivet-Talocia served as Associate Editor for the IEEE TRANSACTIONS ON ELECTROMAGNETIC COMPATIBILITY from 1999 to 2001.

Haisheng Hu received B.Sc and M.A.Sc degrees in electronic engineering in 2006 and 2008 respectively, from Harbin Institute of Technology, Harbin, China. He is currently working toward Ph.D. degree in Electromagnetic Compatibility Group, Politecnico di Torino, Italy. His research interests concern macromodeling of electrical interconnects and related simulation problems. In particular, he works on passive model construction of distributed interconnects and Waveform-Relaxation algorithms.

Piero Triverio (S'06 – M'09) received the M.Sc. and Ph.D. degrees in Electronic Engineering from Politecnico di Torino, Italy in 2005 and 2009, respectively, where He is now a research assistant with the Electromagnetic Compatibility group. In 2005, 2007, and 2009 He visited the Computer Aided Engineering group of Carleton University, Ottawa, Canada. His research interests are in the numerical algorithms for Signal Integrity and Electromagnetic Compatibility analysis and in parallel computing. He received several international awards, including the 2007 Best Paper Award of the IEEE Transactions on Advanced Packaging, the EuMIC Young Engineer Prize of the 13th European Microwave Week, and the Best Paper Award of the IEEE 17th Topical Meeting on Electrical Performance of Electronic Packaging (EPEP 2008).

Dierk Kaller is an Advisory Engineer working in the Systems and Technology Group. He received his Diploma in electrical engineering in 1995 from the University of Hannover, Germany, joining IBM that same year. Since then, he has worked on various System/390 packaging designs in packaging development. He is currently responsible for the signal integrity of the first- and second-level packaging of the zSeries and pSeries high-end servers.

Claudio Siviero received his Diploma in electrical engineering in 2003 and his Ph.D. degree in 2007 from the Politecnico di Torino, Italy. His research activities were in the field of Electromagnetic Compatibility, where he worked on the macromodeling of nonlinear circuit elements with specific application to the behavioral characterization of digital integrated circuits for the assessment of Signal Integrity and Electromagnetic Compatibility effects. In 2008 he joined IBM Development in Boeblingen, Germany. Dr. Siviero's current focus is on electrical packaging design with respect to the Signal Integrity assessment for the pSeries and zSeries.

Martin Kindscher is an Staff Engineer. He received his Diploma and Ph.D. degree in electrical engineering from the Technical University Berlin, Germany. In his current role he is responsible for the signal integrity of ceramic and organic packagings in IBM server systems. His focus is on analysis and simulation of high-speed bus nets.